

## Original Article

**Cite this article:** Zhang Y, Wu Y, Li H, Han J, and Song Q (2023) Genesis of the Jinying gold deposit, southern Jilin Province, NE China: Constraints from geochronology and isotope geochemistry. *Geological Magazine* **160**: 1761–1774. <https://doi.org/10.1017/S0016756823000705>

Received: 2 March 2023

Revised: 8 October 2023

Accepted: 13 October 2023

First published online: 16 November 2023

**Keywords:**

Zircon U–Pb dating; pyrite Rb–Sr dating; isotope geochemistry; Jinying gold deposit; Northeast China

**Corresponding author:**

Yong Zhang; Email: [yongzhangcc@163.com](mailto:yongzhangcc@163.com)

# Genesis of the Jinying gold deposit, southern Jilin Province, NE China: Constraints from geochronology and isotope geochemistry

Yong Zhang<sup>1</sup> , Yushi Wu<sup>2</sup>, Huali Li<sup>3</sup>, Jilong Han<sup>4</sup> and Quanheng Song<sup>5</sup>

<sup>1</sup>MNR Key Laboratory of Metallogeny and Mineral Assessment, Institute of Mineral Resources, Chinese Academy of Geological Sciences, Beijing, China; <sup>2</sup>The Fourth Geological Survey of Jilin Province, Tonghua, China; <sup>3</sup>Institute of Geomechanics, Chinese Academy of Geological Sciences, Beijing, China; <sup>4</sup>State Key Laboratory of Geological Processes and Mineral Resources, China University of Geosciences, Beijing, China and <sup>5</sup>Institute of Geological Survey of Jilin Province, Changchun, China

**Abstract**

The Jinying gold deposit is located in southern Jilin Province in northeast China and is representative of the large Early Cretaceous gold deposits in this area. To better understand ore genesis of this deposit, a multi-isotope integrated analysis of U–Pb–Rb–Sr–He–Ar–S has been carried out. Laser ablation inductively coupled plasma–mass spectrometry (LA–ICP–MS) dating of zircons from the granodiorite porphyry and dioritic porphyrite in the study area yields ages of  $172.1 \pm 1.2$  Ma and  $122.5 \pm 0.8$  Ma, suggesting that corresponding intrusion occurred in the Middle Jurassic and the Early Cretaceous. Rb–Sr dating of the pyrite yields an isochron age of  $120 \pm 3$  Ma, suggesting that gold mineralization occurred in the Early Cretaceous. The fluid inclusions in pyrite yield  $^3\text{He}/^4\text{He}$  ratios clustered within a small range from 0.08 to 0.13 Ra,  $^{40}\text{Ar}/^{36}\text{Ar}$  ratios between 331.6 and 351.3, and mantle He in the range of 1.0–1.6%, indicating that the ore-forming fluids originated from a mixed crustal and mantle source. The in situ S isotopic values of pyrite vary between  $+0.1$  ‰ and  $+2.8$  ‰, suggesting that the ore-related sulphur came from the deep magmatic source. Combined with the geological history of the study area, it can be concluded that the gold mineralization was possibly related to the extensional setting associated with the rollback of the Palaeo-Pacific Plate.

**1. Introduction**

Southern Jilin Province, located in the northeastern margin of the North China Craton (NCC, Fig. 1a), is an important polymetallic metallogenic district that hosts numerous Ni, Fe, Cu and Au deposits (Fig. 1b), and over 20 large-, medium- and small-scale Au deposits have been found in this area. For example, the world-famous Jiapigou gold district contains proven gold reserves of 180 tons or more (Sun *et al.* 2013; Deng *et al.* 2014; Zhang *et al.* 2021; Chen *et al.* 2022). With advanced exploration, several gold deposits have been discovered in southern Jilin Province, including the Songjianghe (Zhang *et al.* 2019), Toudaoliuhe (Han *et al.* 2020), Laosandui and Jinying (known as Banmiaozi) gold deposits. Thus, this area shows great potential for ore prospecting and has been recognized as an important gold province in China.

Jinying is a large-scale gold deposit and currently contains 34 t of gold (Chen, 2019). Previous researches have been focused on the geology (Liu *et al.* 2009; Su & Zang 2010; Xing *et al.* 2012; Li *et al.* 2015), whole-rock geochemistry (Zhang, 2015; Chen, 2019), ore-forming fluid (Zhang, 2015; Men *et al.* 2016; Chen, 2019) and geochronology (Zhang, 2015; Chen, 2019). However, the ore genesis and mineralization time at Jinying deposit remain controversial. For example, Zhang (2015) argued that Au mineralization occurred at 170 Ma based on the zircon U–Pb age of granodiorite porphyry, as well as the zircon U–Pb age of 131 Ma for dioritic porphyrite (Chen, 2019). The deposit formed during the subduction of the Palaeo-Pacific Plate (Zhang, 2015) or in the following extensional setting (Chen, 2019). In addition, the ore-forming fluids originated from a mixture of magmatic water and meteoric water (Men *et al.* 2016) or magmatic water with meteoric water and formation water (Chen, 2019).

In view of the above scientific problems, this work carried out sulphide Rb–Sr and LA–ICP–MS zircon U–Pb geochronological analyses and He–Ar–S isotopic analyses of the Jinying gold deposit. We aim to determine the timing of gold mineralization, tectonic setting and sources of ore-forming materials and fluids, which have important implications for the genesis of the Jinying gold deposit.

© The Author(s), 2023. Published by Cambridge University Press. This is an Open Access article, distributed under the terms of the Creative Commons Attribution licence (<http://creativecommons.org/licenses/by/4.0/>), which permits unrestricted re-use, distribution and reproduction, provided the original article is properly cited.



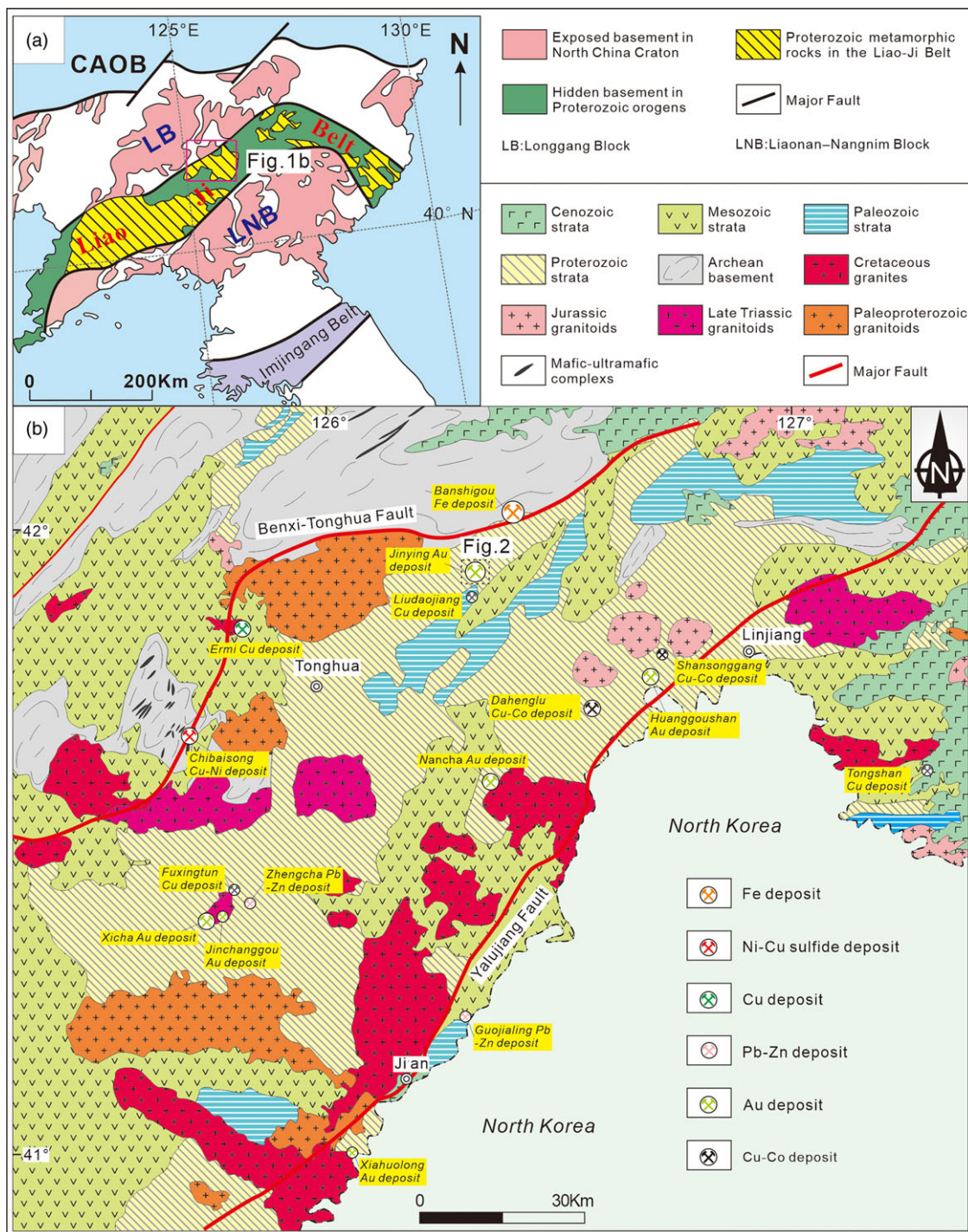


**Figure 1.** (Colour online) (a) Tectonic map of the Proterozoic Liao-Ji belt, northeastern margin of the North China Craton (Zhao et al. 2005); (b) geological map of southern Jilin Province showing the locations of major deposits (Chu et al. 2021).

**2. Geological setting**

The study area is situated between the Liaonan-Nangrim Block and Longgang Block separated by the Palaeoproterozoic Liao-Ji belt (Zhao et al. 2005; Pei et al. 2011, Fig. 1a). The study area underwent multistage cratonization, Palaeoproterozoic rift-subduction-collisional events and late Palaeoproterozoic-Neoproterozoic multistage rifting events that record complicated geotectonic processes in the Precambrian (Zhai, 2013) and final closure of the Palaeo-Asian Ocean in the late Palaeozoic-early

Mesozoic as well as overprinted and modified by Palaeo-Pacific Plate tectonic regimes during the Mesozoic-Cenozoic (Sengör et al. 1993; Sengör & Natal'in, 1996; Wu et al. 2011).

The exposed oldest strata in the study area are Archean TTG rocks, and supracrustal rocks consist of amphibolite, plagiogneiss, granulite and magnetite-quartzite. The Palaeoproterozoic Laoling Group consists of metamorphic conglomerate, quartzite, phyllite, schist and marble. The Neoproterozoic Qingbaikouan System mainly consists of feldspathic quartz sandstone, arkose

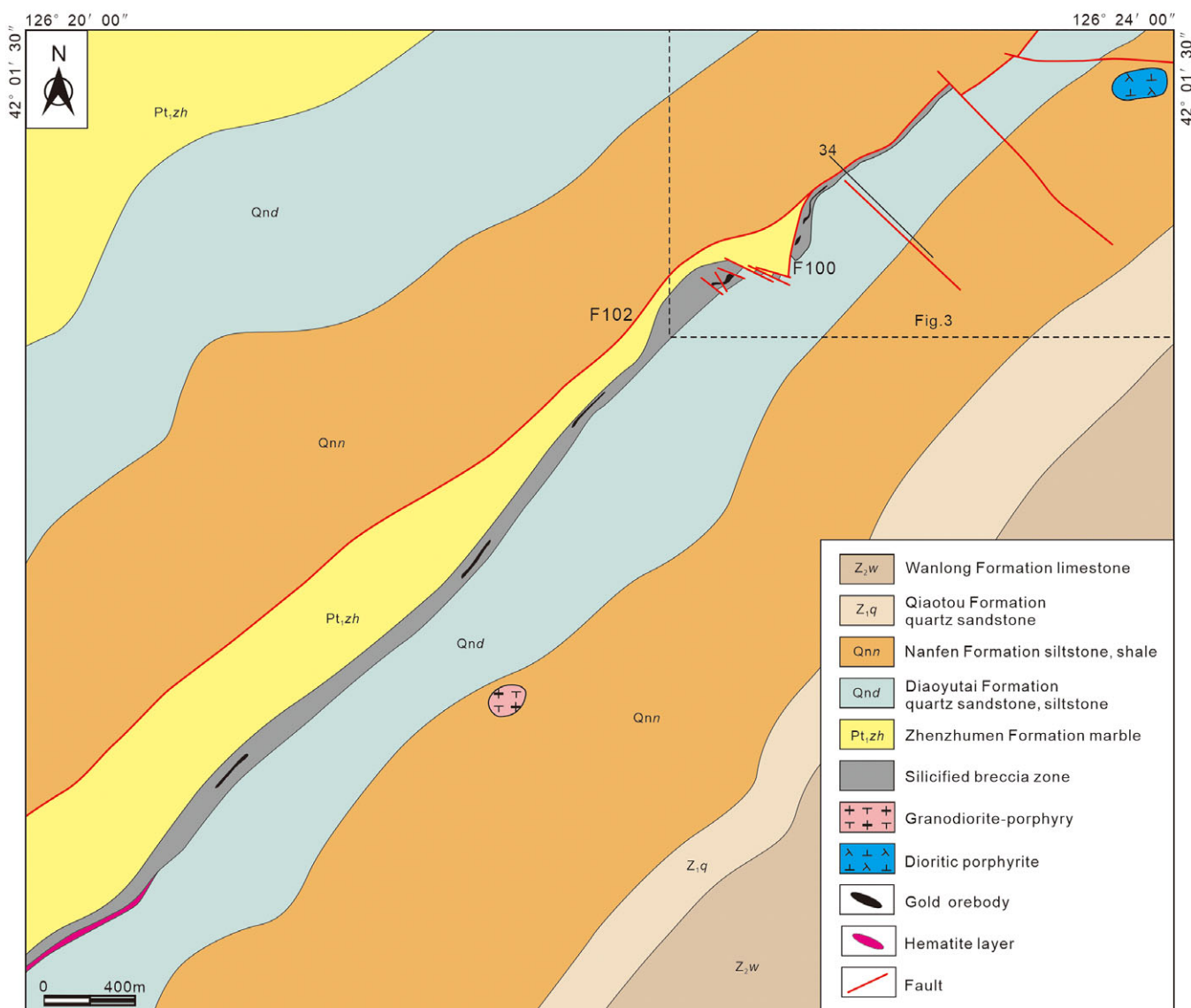
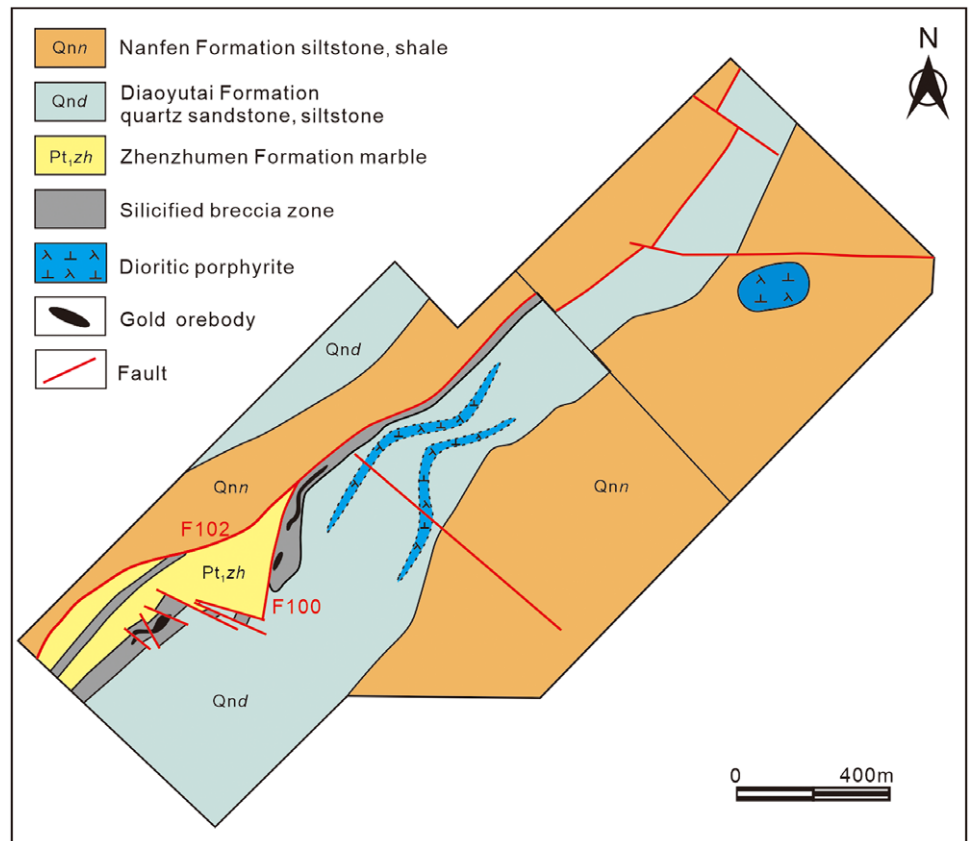


Figure 2. (Colour online) Geological map of the Jinying gold deposit.

and conglomerate. The Jurassic Linzitou and Shiren Formations consist of andesite, andesitic tuff, rhyolite and glutenite. The Cretaceous Xiaonangou Formation sediments consist of conglomerate and glutenite (Fig. 1b). The Quaternary sediments consist of clay and gravel (JBGMR, 1988). The fault system in the study area is dominated by the NE-trending Benxi-Tonghua and Yalujiang faults (Chu *et al.* 2021). Igneous rocks in the area comprise the Late Palaeozoic-Early Mesozoic mafic complex, alkali-granite and associated mafic rocks, and the Mesozoic granitic complex (Zhang, 2002). Mesozoic magmatic activity in the study area can be subdivided into three stages: the Late Triassic, the Early-Middle Jurassic and Cretaceous (Chu *et al.* 2021). Multiple stages of magmatic activity and geotectonic processes formed abundant Au deposits in this area (Sun *et al.* 2006, 2023; Han *et al.* 2022).

### 3. Deposit geology

Proterozoic sediments and metasedimentary rocks are the main rocks in the Jinying gold deposit, and they were subdivided into five units: Palaeoproterozoic Zhenzhumen Formation and Neoproterozoic Diaoyutai, Nanfen, Qiaotou and Wanlong Formations (Fig. 2). The Zhenzhumen Formation is composed of dolomite marble and quartz-bearing dolomite marble. The Diaoyutai Formation occurs in the central and northwest parts of the deposit and is mainly composed of quartz sandstone and hematite-bearing quartz sandstone. The Nanfen Formation is composed of siltstone, micritic limestone and shale. The Qiaotou Formation occurs in the southeastern part of the deposit and is mainly composed of quartz sandstone and siltstone. The Wanlong Formation is mainly exposed in the southeast of the deposit and



**Figure 3.** (Colour online) Geological sketch map of the Jinying gold deposit (Chen *et al.* 2020).

consists mainly of laminated limestone. The structures of the Jinying deposit are dominated by NE- and NW-trending faults, and the NE-trending faults, which are closely related to mineralization. Intrusive rocks in the mining area include granodiorite porphyry and dioritic porphyrite. Granodiorite porphyry is exposed in the south part of the study area (Fig. 2), and dioritic porphyrite is exposed in the northeast part of the study area, as a small-scale rock mass (Fig. 2), but altered dioritic porphyrite can be seen at depth of drill holes 7, 10, 14, 16 and 30 (Fig. 3, Chen *et al.* 2020). Nine orebodies have been discovered in this deposit, and they mainly occur in the silicified breccia zone near the unconformity between the quartz sandstone and the silicified dolomitic marble (Fig. 4). They are controlled spatially by faults of No. F102 and F100 and therefore occur in a bedded shape, with dip SE at 48°–61°, and an average gold grade of 2.33–13.66 g/t (Chen, 2019). The ore minerals comprise native gold (Fig. 5a–d), pyrite (Fig. 5e), marcasite (Fig. 5e), chalcocopyrite (Fig. 5f, g), arsenopyrite, galena, sphalerite, hematite (Fig. 5c, d). Quartz, barite and sericite constitute the gangue mineral association. The alteration types are characterized by silicification, baritization, sericitization, kaolinization and carbonation. The hydrothermal processes can be divided into four paragenetic stages: quartz-pyrite stage, quartz-gold-pyrite stage, barite-chalcedony-gold-hematite stage and pyrite-marcasite stage (Xing *et al.* 2012).

## 4. Samples and analytical methods

### 4.a. Sampling

For zircon U–Pb dating, one granodiorite porphyry sample was collected from an outcrop in the southern part of the deposit, and one dioritic porphyrite sample was collected from tunnel 160. For

the He–Ar isotope analysis, five pyrite samples were collected from tunnel 160. Sixteen pyrite samples were collected from tunnel 365, of which nine for Rb–Sr isotope analyses and seven for in situ sulphur isotope analyses.

Granodiorite porphyry is grey in colour, porphyritic texture and massive structure, and the phenocrysts consist of plagioclase, quartz, biotite and minor K-feldspar and hornblende. The plagioclase crystals are platy with lengths varying from 0.5 to 3 mm and are characterized by sericitization. The K-feldspar grains anhedral with lengths varying from 1 to 2 mm. The quartz grains show anhedral shape with lengths varying from 0.5 to 8 mm. The matrix is composed of quartz, feldspar and biotite, with minor accessory magnetite, zircon and apatite (Fig. 5h). Dioritic porphyrite is grey, porphyritic texture, massive structure, and the phenocrysts are mainly plagioclase, quartz, biotite and hornblende. The plagioclase crystals are platy with lengths varying from 1 to 10 mm and are characterized by sericitization. The quartz grains are xenomorphic with lengths varying from 0.5 to 5 mm. The biotite is platy with lengths varying from 0.5 to 2 mm and is characterized by chloritization. The hornblende crystals are rhombic with lengths varying from 0.5 to 5 mm. The matrix is composed of quartz, plagioclase and biotite, with minor accessory magnetite, zircon and apatite (Fig. 5i).

### 4.b. Analytical methods

#### 4.b.1. Zircon U–Pb dating

Zircon grains were separated using conventional heavy liquid and magnetic techniques, followed by hand selection under a binocular microscope. U–Pb isotopic analyses were performed using an Agilent 7500 mass spectrometer connected to a 193 nm ArF excimer laser ablation system at the MNR Key Laboratory of

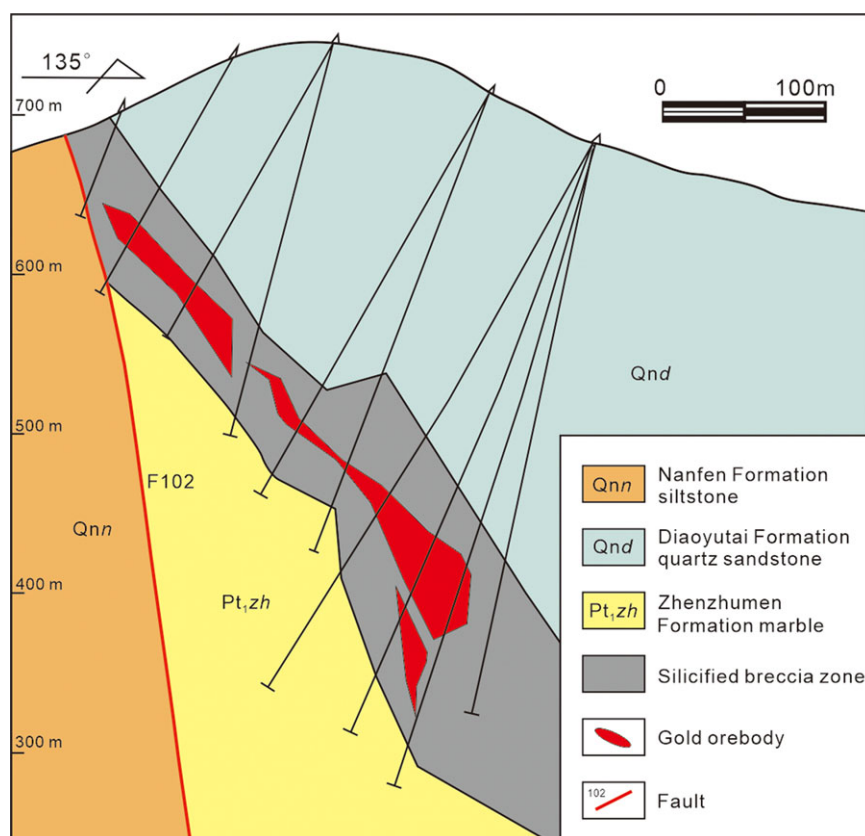


**Figure 4.** (Colour online) Cross-section showing the geology along exploration Line 34.

Metallogeny and Mineral Assessment, Institute of Mineral Resources, Chinese Academy of Geological Sciences (CAGS). Detailed operating conditions for the laser ablation system, the LA-ICP-MS instrument and data reduction were described by Hou *et al.* (2009). Errors in individual analyses by LA-ICP-MS are provided at the  $1\sigma$  level, while errors in pooled ages are noted at the 95% confidence level. Concordia diagrams and weighted mean calculations were made using the Isoplot program (Ludwig, 2003).

#### 4.b.2. Rb-Sr isotope analysis

The samples were crushed to a 40–80 mesh size and hand-selected under a binocular microscope, yielding samples of >99% purity. Sulphide grains were crushed to a <200 mesh size before analysis and then washed in an ultrasonic bath and dried. Rb and Sr isotopic analyses were performed on a VG-354 mass spectrometer with five collectors at the Nantai Geological Testing Institute, Nanjing, China. The analytical procedures were consistent with those described by Wang *et al.* (2007a, 2007b). During analysis, the reproducibility and accuracy of Sr isotope measurements were periodically checked by running the NBS987 standard reference material and laboratory standard La Jolla with a mean  $^{87}\text{Sr}/^{86}\text{Sr}$  value of  $0.710342 \pm 0.000040$  (certified value:  $0.710340 \pm 0.000260$ ) based on the standard  $^{86}\text{Sr}/^{88}\text{Sr} = 0.1194$ . The accuracy of the Rb/Sr ratios was better than 1%.

#### 4.b.3. He-Ar isotope analysis

He-Ar isotopic analyses of five pyrite samples were conducted using a Helix SFT noble gas isotope mass spectrometer at the MNR Key Laboratory of Metallogeny and Mineral Assessment, Institute of Mineral Resources, CAGS. The measurement procedure

consisted of crushing, purification and mass spectrometry. All weighed pyrite samples were measured under high vacuum conditions for analysis, with  $n \times 10^{-9}$  mbar in the crush and purification system and  $n \times 10^{-10}$  mbar in the mass spectrometer system. The details can be found in Liu *et al.* (2018).

#### 4.b.4. In situ S isotope

Seven pyrite samples (BMZ6, BMZ7, BMZ8, BMZ9, BMZ10, BMZ13, BMZ14) for in situ sulphur isotope analyses were analysed using a laser ablation coupled multicollector inductively coupled plasma mass spectrometer (LA-MC-ICP-MS) at the MNR Key Laboratory of Metallogeny and Mineral Assessment, Institute of Mineral Resources, CAGS. The laser fluence was  $5.0 \text{ J/cm}^2$ , with a frequency of 4 Hz and spot diameter of 40–50  $\mu\text{m}$ . The ablation method consisted of single-point ablation with a high-purity carrier gas. A standard-sample bracketing method (SSB) was employed to correct for instrumental mass fractionation, calibrated via a Baltat pyrite standard (Crowe & Vaughan, 1996), and the matrix effect was no more than 0.5%.

## 5. Results

### 5.a. LA-ICP-MS zircon U-Pb ages

The zircons are euhedral or subhedral and show oscillatory zoning (Fig. 6a, b). The results of LA-ICP-MS zircon U-Pb dating are presented in Table 1. The zircon grains collected from granodiorite porphyry (BMZ-2) yield  $^{206}\text{Pb}/^{238}\text{U}$  ages of 170.1–173.9 Ma and yield a zircon U-Pb concordia age and weighted age of  $171.9 \pm 0.5 \text{ Ma}$  and  $172.1 \pm 1.2 \text{ Ma}$ , respectively (Fig. 7a, b). The zircon grains collected from dioritic porphyrite (BMZ-5) yield  $^{206}\text{Pb}/^{238}\text{U}$  ages of 120.1–2478 Ma (Fig. 7c). A total of 15 zircon grains of

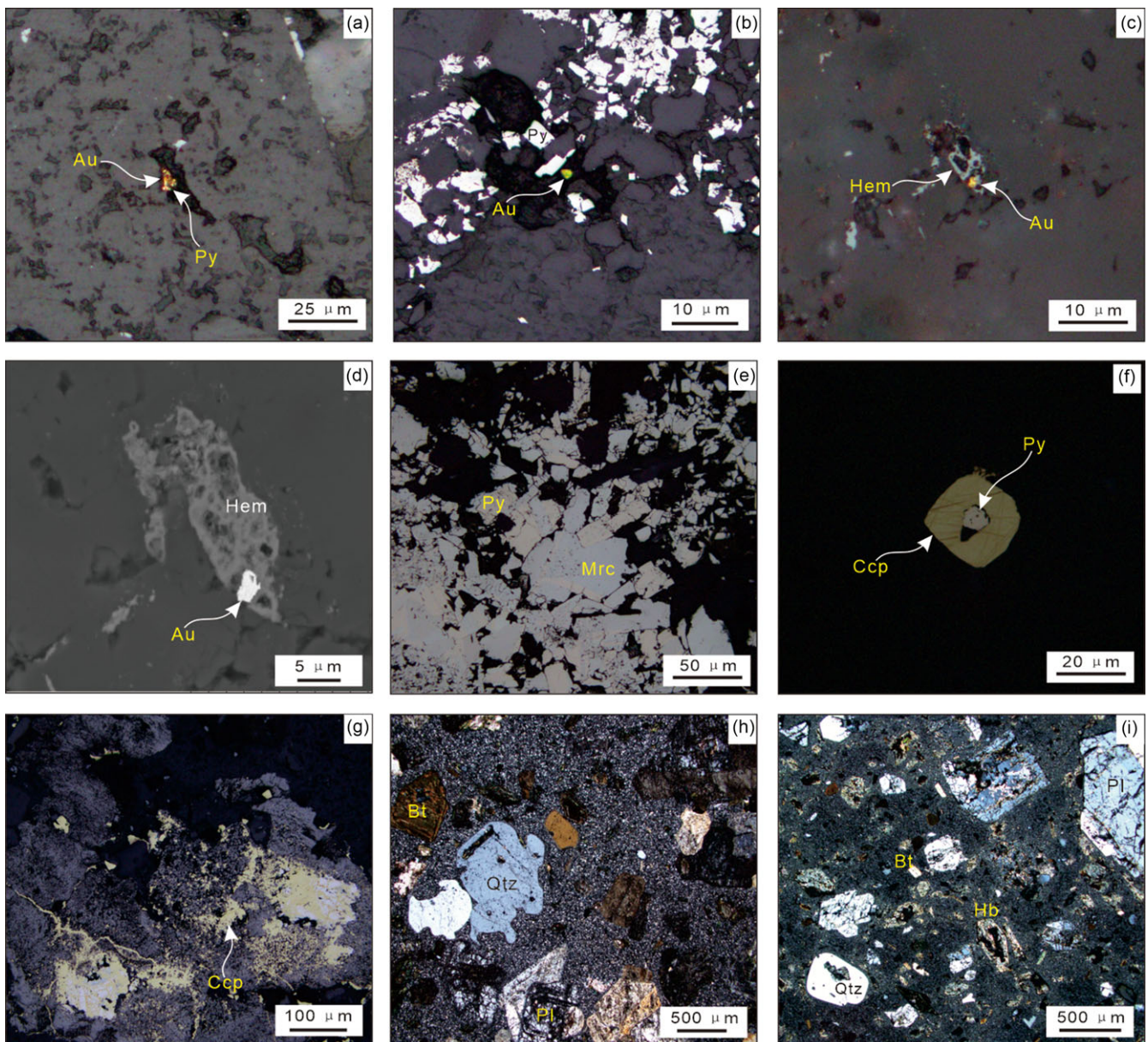


**Figure 5.** (Colour online) Photomicrographs of the Jinying gold deposit. (a, b) Gold coexisting with pyrite (reflected light); (c, d) gold coexisting with hematite (c-reflected light, d-BSE); (e) pyrite coexisting with marcasite (reflected light); (f) chalcopyrite coexisting with pyrite (reflected light); (g) chalcopyrite mineralization (reflected light); (h) granodiorite porphyry (cross-polarized light); (i) dioritic porphyry (cross-polarized light). Hem = hematite; Au = gold; Py = pyrite; Mrc = marcasite; Ccp = chalcopyrite; Bt = biotite; Qtz = quartz; Hb = hornblende; Pl = plagioclase.

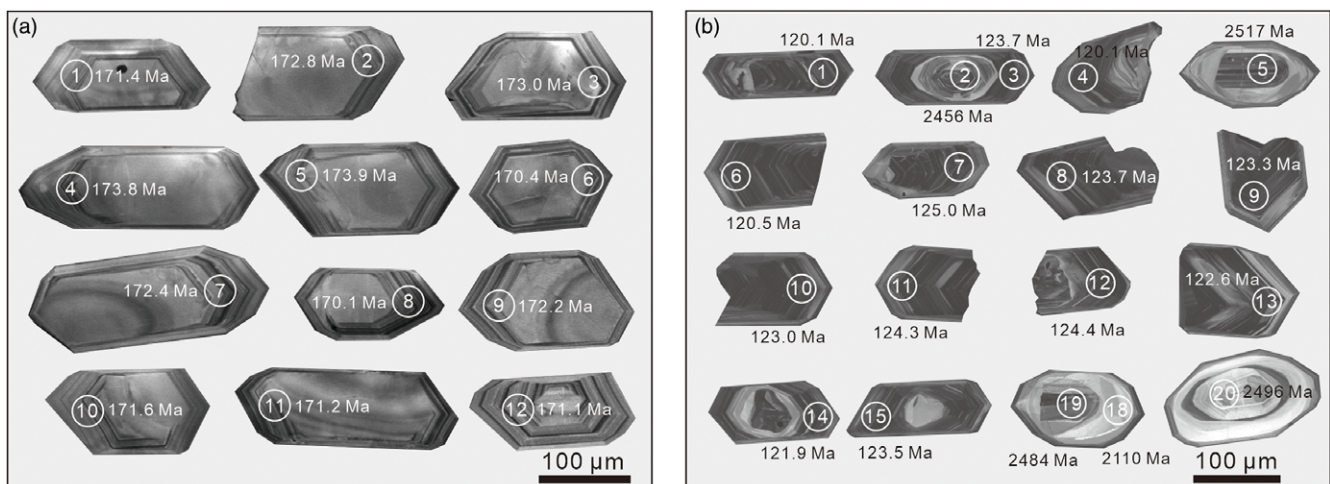


**Figure 6.** Representative CL images of analysed zircons extracted from granodiorite porphyry and dioritic porphyry in the Jinying gold deposit.

**Table 1.** LA-ICP-MS zircon U–Pb dating results of intrusions in the Jinying gold deposit

Sample No.	$^{207}\text{Pb}/^{206}\text{Pb}$	1 $\sigma$	$^{207}\text{Pb}/^{235}\text{U}$	1 $\sigma$	$^{206}\text{Pb}/^{238}\text{U}$	1 $\sigma$	$^{207}\text{Pb}/^{206}\text{U}$	1 $\sigma$	$^{207}\text{Pb}/^{235}\text{U}$	1 $\sigma$	$^{206}\text{Pb}/^{238}\text{U}$	1 $\sigma$
BMZ-2												
BMZ-2-1	0.04973	0.00324	0.18471	0.01179	0.02695	0.00036	189.0	147.2	172.1	10.1	171.4	2.3
BMZ-2-2	0.04977	0.00393	0.18561	0.01385	0.02717	0.00065	183.4	183.3	172.9	11.9	172.8	4.1
BMZ-2-3	0.05065	0.00587	0.18654	0.02206	0.02720	0.00089	233.4	238.9	173.7	18.9	173.0	5.6
BMZ-2-4	0.05083	0.00307	0.18677	0.01083	0.02732	0.00045	231.6	140.7	173.9	9.3	173.8	2.8
BMZ-2-5	0.04978	0.00195	0.18618	0.00716	0.02735	0.00028	183.4	86.1	173.4	6.1	173.9	1.8
BMZ-2-6	0.05074	0.00459	0.18357	0.01549	0.02678	0.00061	227.8	213.9	171.1	13.3	170.4	3.8
BMZ-2-7	0.05133	0.00336	0.18550	0.01128	0.02710	0.00052	253.8	150.0	172.8	9.7	172.4	3.3
BMZ-2-8	0.05012	0.00218	0.18277	0.00805	0.02674	0.00033	211.2	100.0	170.4	6.9	170.1	2.0
BMZ-2-9	0.04977	0.00225	0.18511	0.00856	0.02707	0.00033	183.4	105.5	172.4	7.3	172.2	2.1
BMZ-2-10	0.04795	0.00532	0.18350	0.02093	0.02698	0.00055	98.2	240.7	171.1	18.0	171.6	3.5
BMZ-2-11	0.04666	0.00695	0.18437	0.02528	0.02691	0.00042	31.6	322.2	171.8	21.7	171.2	2.6
BMZ-2-12	0.04858	0.00542	0.18313	0.02014	0.02689	0.00039	127.9	244.4	170.8	17.3	171.1	2.5
BMZ-2-13	0.05022	0.00284	0.18508	0.01068	0.02677	0.00043	205.6	126.8	172.4	9.2	170.3	2.7
BMZ-2-14	0.04996	0.00159	0.18659	0.00560	0.02726	0.00026	194.5	74.1	173.7	4.8	173.4	1.6
BMZ-2-15	0.04931	0.00183	0.18441	0.00718	0.02703	0.00031	161.2	91.7	171.9	6.2	171.9	1.9
BMZ-2-16	0.05082	0.00350	0.18451	0.01194	0.02675	0.00053	231.6	159.2	171.9	10.2	170.2	3.3
BMZ-2-17	0.05078	0.00520	0.18712	0.01730	0.02690	0.00072	231.6	218.5	174.2	14.8	171.1	4.5
BMZ-2-18	0.05038	0.00287	0.18519	0.01024	0.02711	0.00039	213.0	131.5	172.5	8.8	172.4	2.5
BMZ-5												
BMZ-5-1	0.04948	0.00345	0.12981	0.00778	0.01880	0.00054	168.6	155.5	123.9	7.0	120.1	3.4
BMZ-5-2	0.15902	0.00396	9.92997	0.12566	0.45744	0.01623	2456	42	2428	12	2428	72
BMZ-5-3	0.04815	0.00173	0.12877	0.00468	0.01937	0.00022	105.6	85.2	123.0	4.2	123.7	1.4
BMZ-5-4	0.04879	0.00049	0.12624	0.00135	0.01880	0.00016	200.1	19.4	120.7	1.2	120.1	1.0
BMZ-5-5	0.16590	0.00186	9.72750	0.77906	0.45217	0.04361	2517	19	2409	74	2405	194
BMZ-5-6	0.04855	0.00262	0.12553	0.00668	0.01886	0.00024	127.9	127.8	120.1	6.0	120.5	1.5
BMZ-5-7	0.04815	0.00233	0.13085	0.00886	0.01958	0.00078	105.6	111.1	124.9	8.0	125.0	4.9
BMZ-5-8	0.04824	0.00054	0.12881	0.00162	0.01937	0.00018	109.4	58.3	123.0	1.5	123.7	1.1
BMZ-5-9	0.04909	0.00161	0.12958	0.00423	0.01931	0.00039	153.8	77.8	123.7	3.8	123.3	2.4
BMZ-5-10	0.04889	0.00200	0.12952	0.00537	0.01926	0.00022	142.7	96.3	123.7	4.8	123.0	1.4
BMZ-5-11	0.04838	0.00161	0.13022	0.00434	0.01947	0.00024	116.8	77.8	124.3	3.9	124.3	1.5

(Continued)

Table 1. (Continued)

Sample No.	$^{207}\text{Pb}/^{206}\text{Pb}$	$1\sigma$	$^{207}\text{Pb}/^{235}\text{U}$	$1\sigma$	$^{206}\text{Pb}/^{238}\text{U}$	$1\sigma$	$^{207}\text{Pb}/^{206}\text{U}$	$1\sigma$	$^{207}\text{Pb}/^{235}\text{U}$	$1\sigma$	$^{206}\text{Pb}/^{238}\text{U}$	$1\sigma$
BMZ-5-12	0.04821	0.00100	0.12919	0.00235	0.01948	0.00030	109.4	52.8	123.4	2.1	124.4	1.9
BMZ-5-13	0.04823	0.00059	0.12832	0.00188	0.01920	0.00015	109.4	29.6	122.6	1.7	122.6	1.0
BMZ-5-14	0.04857	0.00222	0.12843	0.00566	0.01909	0.00043	127.9	107.4	122.7	5.1	121.9	2.7
BMZ-5-15	0.04785	0.00232	0.12868	0.00650	0.01934	0.00048	100.1	111.1	122.9	5.8	123.5	3.0
BMZ-5-16	0.04925	0.00244	0.12888	0.00835	0.01891	0.00079	166.8	116.7	123.1	7.5	120.8	5.0
BMZ-5-17	0.04985	0.00327	0.12962	0.00876	0.01914	0.00041	187.1	155.5	123.8	7.9	122.2	2.6
BMZ-5-18	0.13092	0.00831	7.58244	1.05876	0.39402	0.04398	2110	111	2183	126	2141	203
BMZ-5-19	0.16266	0.00111	10.38890	0.10940	0.46214	0.00450	2484	11	2470	10	2449	20
BMZ-5-20	0.16385	0.00152	10.60484	0.15349	0.46872	0.00577	2496	21	2489	13	2478	25

dioritic porphyrite yield  $^{206}\text{Pb}/^{238}\text{U}$  ages of 120.1–125.0 Ma and yield a zircon U–Pb concordia age and weighted age of  $122.5 \pm 0.4$  Ma and  $122.5 \pm 0.8$  Ma, respectively (Fig. 7d). The remaining zircon grains yields ages of 2141–2478 Ma; they are interpreted as inherited ones.

### 5.b. Rb–Sr dating

The Rb and Sr concentrations for nine pyrite samples from the Jinying gold deposit are listed in Table 2. The Rb contents of pyrite range from 1.268 to 3.519 ppm, and the Sr contents ranging from 1.249 to 104.5 ppm. The  $^{87}\text{Rb}/^{86}\text{Sr}$  values range from 0.103 to 2.963. Nine data points yield an imprecise age of  $123 \pm 29$  Ma with an initial  $^{87}\text{Sr}/^{86}\text{Sr}$  ratio of  $0.7109 \pm 0.0007$  ( $n = 9$ , MSWD = 78; Fig. 8a), which is considered unreliable. By removing three discrete points (BM-2, BM-3, and BM-9), the remaining data points yield a more precise date of  $120 \pm 3$  Ma with an initial  $^{87}\text{Sr}/^{86}\text{Sr}$  ratio of  $0.7108 \pm 0.00007$  (MSWD = 1.4; Fig. 8b).

### 5.c. He–Ar isotopes

The He–Ar isotopic results of pyrite samples are presented in Table 3. The concentrations of  $^4\text{He}$  and  $^3\text{He}$  are  $(27.20\text{--}41.66) \times 10^{-7}$  cm<sup>3</sup>STP/g and  $(41.20\text{--}65.91) \times 10^{-14}$  cm<sup>3</sup>STP/g, respectively, and  $^{40}\text{Ar}$  ranges from  $189.32 \times 10^{-8}$  cm<sup>3</sup>STP/g to  $336.40 \times 10^{-8}$  cm<sup>3</sup>STP/g. The  $^{40}\text{Ar}/^{36}\text{Ar}$  ratios are 331.6–351.3. The  $^3\text{He}/^4\text{He}$  ratios vary from  $1.17 \times 10^{-7}$  to  $1.87 \times 10^{-7}$ . The R/Ra ratios of the ore-forming fluid from the pyrite samples are 0.08–0.13.

### 5.d. In situ S isotopic compositions

The in situ S isotopic compositions of pyrite are listed in Table 4. The  $\delta^{34}\text{S}$  values of pyrite have a relatively narrow range from +0.1 ‰ to +2.8 ‰ (Fig. 9a, b) and an average of 1.6 ‰ ( $n = 24$ ).

## 6. Discussion

### 6.a. Timing of gold mineralization

The volume of dioritic porphyrite increases towards deep levels, suggesting a considerable flux of dioritic magmas (Chen *et al.* 2020). At the No. 7 drill hole, the dioritic porphyrite is featured by sericitization and kaolinization at a depth of 51 metres. On either side in contact with the gold-bearing silicified breccia, the mineralized alteration shows a gradual trend of evolution from strong to weak. Moreover, mineralized altered dioritic porphyrite breccia was found in drill holes 10, 14, 16 and 30. All these ideological facts show that the genesis of the gold deposit is closely related to the dioritic porphyrite. In this study, the Rb–Sr age of  $120 \pm 3$  Ma for pyrite associated with Au mineralization in the ore vein provides evidence of an Early Cretaceous Au mineralization age. Zircon U–Pb dating indicates that the crystallization age of the dioritic porphyrite was  $122.5 \pm 0.8$  Ma, whereas the granodiorite porphyry yielded a relatively older age of  $172.1 \pm 1.2$  Ma. These ages indicate that dioritic porphyrite and gold mineralization were largely synchronous and that mineralization and magmatism occurred in the Early Cretaceous. The age interpreted for the Jinying deposit is similar to that of many other magmatic-hydrothermal ore deposits in eastern Liaoning and southern Jilin. These include the Wulong Au deposit (119 Ma, Zhang *et al.* 2020), Xinfang Au deposit (121 Ma, Zhang *et al.* 2022a), Changfagou Cu (Au) deposit (116 Ma; Zhang *et al.* 2017) and Tianhexing Cu (Mo) deposit (115 Ma; Zhang *et al.* 2015). The Jinying Au deposit is thus

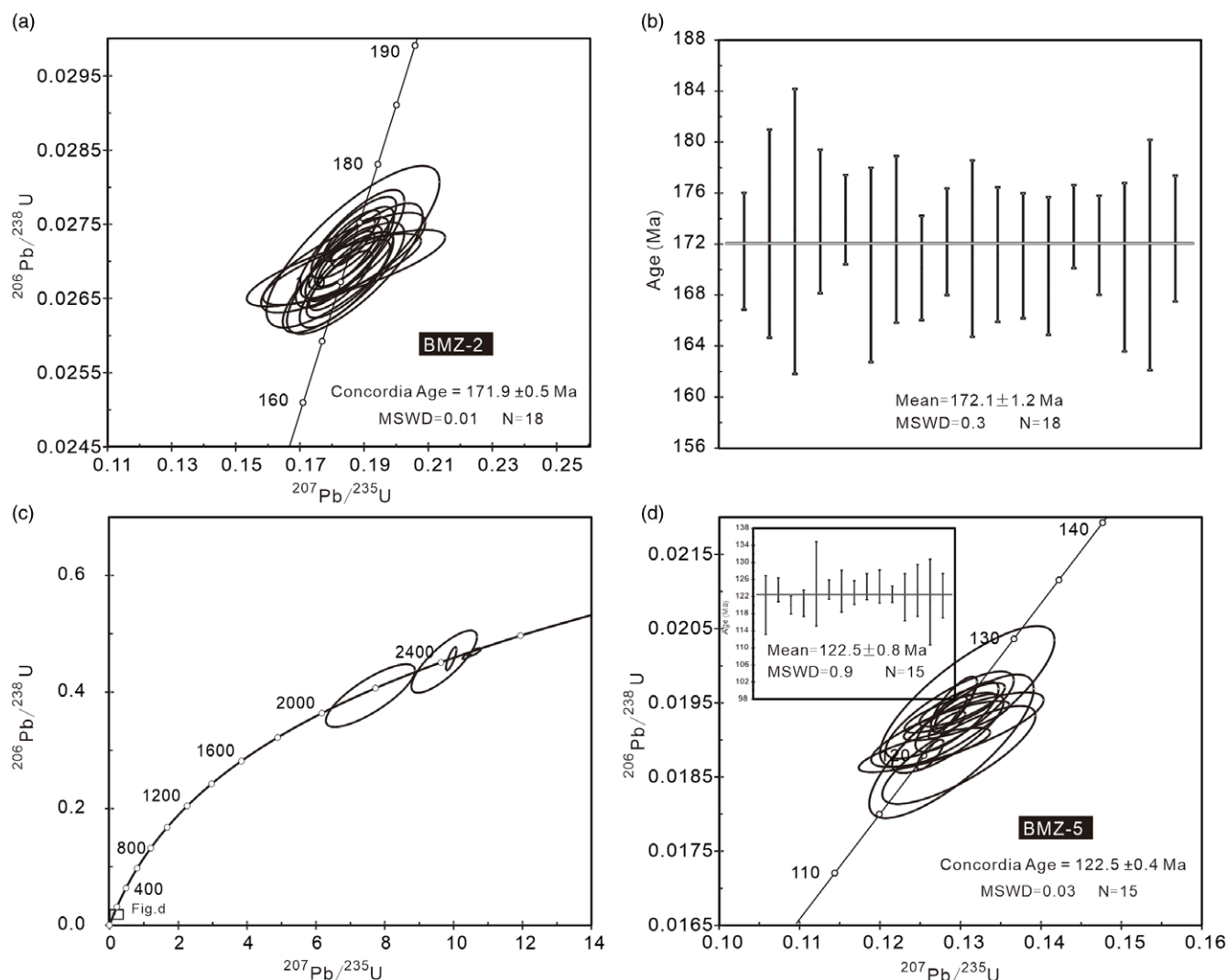


Figure 7. Zircon U-Pb concordia diagrams for samples BMZ-2 (a, b) and BMZ-5 (c, d) from the Jinying gold deposit.

representative of an important Early Cretaceous gold mineralization event in southern Jilin Province.

### 6.b. Source of sulphur and ore-forming fluids

The  $\delta^{34}\text{S}$  values of pyrite at Jinying show a narrow range from +0.1‰ to +2.8‰ (mean = 1.6‰,  $n = 24$ ), which are consistent with those from the typical magmatic-hydrothermal deposit worldwide ( $0 \pm 3$ ‰, Ohmoto & Rye 1979) and from magmatic-hydrothermal Au deposits in the Liaodong Peninsula (e.g. Wulong, Liu *et al.* 2019, Zhang *et al.* 2020; Xinfang, Zhang *et al.* 2022a). These data indicate that the sulphur of the Jinying deposit was derived from a magmatic source.

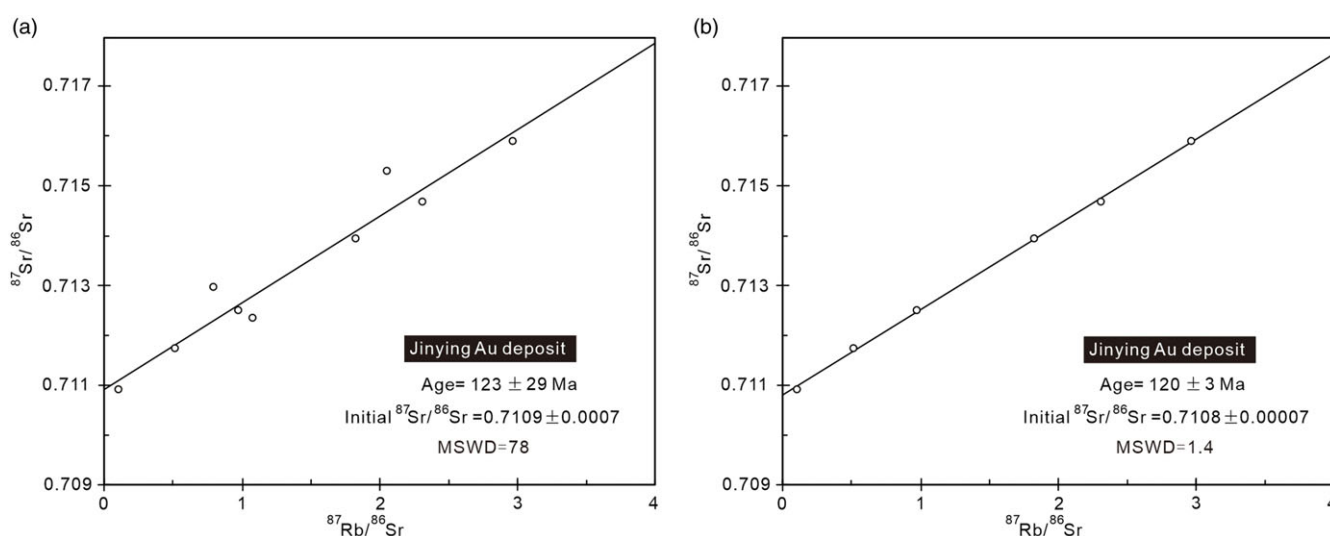
It is generally recognized that there are three potential sources of He and Ar isotopes (Turner *et al.* 1993; Stuart *et al.* 1995; Burnard *et al.* 1999): (1) air-saturated water (ASW, e.g. meteoric water or seawater) with a  $^3\text{He}/^4\text{He}$  ratio of  $1\text{Ra} = 1.4 \times 10^{-6}$  and a  $^{40}\text{Ar}/^{36}\text{Ar}$  ratio of 295.5; (2) mantle-derived fluids with  $^3\text{He}/^4\text{He}$  ratios generally of 6–9 Ra and  $^{40}\text{Ar}/^{36}\text{Ar} > 40000$ ; and (3) crust-derived fluids with  $^3\text{He}/^4\text{He}$  ratios of 0.01 to 0.05 Ra and  $^{40}\text{Ar}/^{36}\text{Ar} > 45000$ . The  $^3\text{He}/^4\text{He}$  ratios of the pyrite from Jinying range from

0.08 to 0.13 Ra, which are slightly higher than those of crust-derived fluids. In the plot of  $^3\text{He}$  vs.  $^4\text{He}$  (Fig. 10a), all of the data are located between the crust and mantle helium isotopic compositions, indicating that the ore-forming fluids of the Jinying gold deposit were derived from mixed mantle and crustal sources.

For Ar isotopes, the obtained  $^{40}\text{Ar}/^{36}\text{Ar}$  values of fluid inclusions range from 331.6 to 351.3 and are slightly higher than those of ASW (295.5, Fig. 10b). In the  $^3\text{He}/^4\text{He}$  (R/Ra) vs.  $^{40}\text{Ar}/^{36}\text{Ar}$  diagram (Fig. 10b), all of the data plot between the crustal and mantle end-members, indicating that the ore-forming fluids might be a mixture of two end-member fluids. These He–Ar isotope data are similar to those from the Early Cretaceous magmatic-hydrothermal Au deposits in the Liaodong. Likewise, the  $^3\text{He}/^4\text{He}$  and  $^{40}\text{Ar}/^{36}\text{Ar}$  values of pyrite from Wulong range from 0.15–0.54 R/Ra and 297–315 (Zhang *et al.* 2020). For the Xinfang gold deposit, the  $^3\text{He}/^4\text{He}$  and  $^{40}\text{Ar}/^{36}\text{Ar}$  values of pyrite range from 0.14–0.62 R/Ra and 1008–7100 (Zhang *et al.* 2022a). Moreover, the proportion of mantle  $^4\text{He}$  is calculated as  $\text{He}_{\text{mantle}} (\%) = (\text{R}_{\text{sample}} - \text{R}_{\text{crust}}) / (\text{R}_{\text{mantle}} - \text{R}_{\text{crust}}) \times 100\%$ , where  $\text{R}_{\text{mantle}} = 8$ ,  $\text{R}_{\text{crust}} = 0.01$  and R represents the  $^3\text{He}/^4\text{He}$  ratios of the fluids in the mantle, crust, and sample (Tolstikhin, 1978; Kendrick *et al.* 2001). The calculated

**Table 2.** Rb-Sr isotopic analyses of pyrite from the Jinying gold deposit

Sample no.	Mineral	Rb ( $\mu\text{g/g}$ )	Sr ( $\mu\text{g/g}$ )	$^{87}\text{Rb}/^{86}\text{Sr}$	$^{87}\text{Sr}/^{86}\text{Sr}$
BM-8	Pyrite	1.392	8.036	0.5128	0.711742 $\pm$ 8
BM-9	Pyrite	2.407	8.953	0.7902	0.712984 $\pm$ 13
BM-10	Pyrite	3.519	9.662	1.0750	0.712361 $\pm$ 15
BM-11	Pyrite	1.268	1.249	2.9630	0.715893 $\pm$ 7
BM-16	Pyrite	1.835	5.578	0.9716	0.712505 $\pm$ 9
BM-17	Pyrite	1.602	2.057	2.3080	0.714679 $\pm$ 8
BM-18	Pyrite	1.394	2.279	1.8240	0.713943 $\pm$ 7
BM-19	Pyrite	3.407	104.5	0.1029	0.710917 $\pm$ 9
BM-20	Pyrite	2.816	4.032	2.0510	0.715327 $\pm$ 11

**Figure 8.** Plot of sulphide Rb-Sr isochron for the Jinying gold deposit.

results indicate a mantle He range of 1.0–1.6%, indicating that the ore-forming fluids were dominantly crustal fluids with inputs of minor amounts of mantle fluids.

### 6.c. Ore genesis and tectonic implications

The sulphur isotopic compositions of pyrite suggested that the sulphur of the Jinying gold deposit has a magmatic source. Their He-Ar isotopic compositions suggest that the ore-forming fluids were derived from mixed mantle and crustal sources. The timing of gold mineralization is similar to the timing of emplacement of spatially related dioritic porphyrite in the deposit, implying that the mineralization was related to the intrusive activity. Based on the above arguments, it is reasonable to interpret the Jinying gold deposit is a magmatic-hydrothermal deposit.

The study area is located within the eastern edge of the NCC, which records the evolution and the final closure of the Palaeo-Asian Ocean, as well as the overprinting of the Palaeo-Pacific tectonic regimes during the Mesozoic (Sengör *et al.* 1993; Sengör & Natal'in, 1996; Li, 2006; Wu *et al.* 2011; Xu *et al.* 2013). Multiple stages and complicated geotectonic processes led to the formation of abundant magnesite, talcum, boron, lead-zinc and gold deposits in this area (Shen *et al.* 2020; Li *et al.* 2023; Zhang *et al.* 2023). The

northern margin of the NCC is the most important gold belt in China, and many previous studies have examined the mineralization age and tectonic setting of gold deposits. The results show that gold mineralization occurred in the Permian-Triassic, Jurassic and Early Cretaceous (Li *et al.* 2018; Zeng *et al.* 2021; Zhang *et al.* 2022b; Song *et al.* 2023; Zhao *et al.* 2023), formed during closure of the Palaeo-Asian Ocean, subduction of the Palaeo-Pacific Plate and an extensional setting associated with rollback of the Palaeo-Pacific Plate (Zhu *et al.* 2015; Wu *et al.* 2019), respectively. In this study, we determined that magmatism and mineralization at Jinying occurred during the Early Cretaceous, and the formation of the deposit likely occurred in an extensional setting controlled by the rollback of the Palaeo-Pacific Plate. This interpretation is extensional-related settings, lithospheric thinning and delamination occurring spatially from west to the east with accompanying by upwelling asthenospheric mantle. In this case, the hot asthenospheric mantle provided enough heat to melt the delaminated lower crust and react with it, producing adakitic magmas in this area (Chen *et al.* 2020; Xuan *et al.* 2022), where magmatic differentiation formed ore-bearing fluids. The ore-bearing fluids then ascended along the fault and mixed with meteoric water or metamorphic water, which was accompanied by complicated physical and chemical changes that would have led to

**Table 3.** He-Ar isotopic compositions of fluid inclusions trapped in pyrite from the Jinying gold deposit

Sample	Mineral	$^4\text{He}(10^{-7})$ ( $\text{cm}^3\text{STP/g}$ )	$^{40}\text{Ar}(10^{-8})$ ( $\text{cm}^3\text{STP/g}$ )	$^{40}\text{Ar}/^{36}\text{Ar}$	$^3\text{He}/^4\text{He}(10^{-7})$	$^{36}\text{Ar}(10^{-7})$	$^{36}\text{Ar}/^{38}\text{Ar}$	$^3\text{He}(10^{-14})$	R/Ra
20JY3-1	Pyrite	37.82	336.40	337.9	1.74	0.996	5.37	65.91	0.12
20JY3-2	Pyrite	27.20	268.38	331.6	1.87	0.809	5.34	50.91	0.13
20JY3-3	Pyrite	27.54	189.32	341.7	1.50	0.554	5.34	41.20	0.11
20JY3-4	Pyrite	41.66	189.58	351.3	1.17	0.540	5.35	48.64	0.08
20JY3-5	Pyrite	34.13	227.07	338.4	1.25	0.671	5.35	42.68	0.09

Note:  $R/Ra = (^3\text{He}/^4\text{He})_{\text{sample}}/1.4 \times 10^{-6}$ .

**Table 4.** In situ sulphur isotope results of ore minerals in the Jinying gold deposit

Sample No.	Sample description	Mineral	$\delta^{34}\text{S}$ (‰)
BMZ6-1	Quartz-pyrite vein	Pyrite	1.5
BMZ6-2	Quartz-pyrite vein	Pyrite	2.2
BMZ6-3	Quartz-pyrite vein	Pyrite	1.9
BMZ7-1	Quartz-pyrite vein	Pyrite	2.0
BMZ7-2	Quartz-pyrite vein	Pyrite	2.5
BMZ7-3	Quartz-pyrite vein	Pyrite	2.8
BMZ8-1	Quartz-pyrite vein	Pyrite	2.4
BMZ8-1	Quartz-pyrite vein	Pyrite	2.1
BMZ8-1	Quartz-pyrite vein	Pyrite	2.5
BMZ9-1	Gold-pyrite ores	Pyrite	1.5
BMZ9-2	Gold-pyrite ores	Pyrite	1.5
BMZ9-3	Gold-pyrite ores	Pyrite	1.9
BMZ10-1	Gold-pyrite ores	Pyrite	2.1
BMZ10-1	Gold-pyrite ores	Pyrite	0.1
BMZ10-3	Gold-pyrite ores	Pyrite	1.5
BMZ13-1	Gold-pyrite ores	Pyrite	0.2
BMZ13-2	Gold-pyrite ores	Pyrite	0.9
BMZ13-3	Gold-pyrite ores	Pyrite	1.5
BMZ14-1	Pyrite-marcasite	Pyrite	1.6
BMZ14-2	Pyrite-marcasite	Pyrite	2.0
BMZ14-3	Pyrite-marcasite	Pyrite	1.6
BMZ14-4	Pyrite-marcasite	Pyrite	0.9
BMZ14-5	Pyrite-marcasite	Pyrite	0.5
BMZ14-6	Pyrite-marcasite	Pyrite	0.5

the deposition of gold and metal sulphides in the structural breccia belt.

## 7. Conclusions

- (1) Zircons from granodiorite porphyry and dioritic porphyry yield U–Pb ages of  $172.1 \pm 1.2$  Ma and  $122.5 \pm 0.8$  Ma, respectively, and the Rb–Sr isotopic age is  $120 \pm 3$  Ma for pyrite samples associated with gold, indicating that gold mineralization and associated magmatism of the Jinying gold deposit occurred during the Early Cretaceous.
- (2) He–Ar isotopic compositions indicate that the ore-forming fluids mainly originated from a mixture of crustal and mantle components. In situ S isotope compositions of pyrite indicate that the ore-related sulphur source was derived from deep magma.
- (3) The Early Cretaceous diagenesis and mineralization formed in an extensional setting associated with rollback of the Palaeo-Pacific Plate.

**Acknowledgements.** This work was jointly supported by the Science & Technology Fundamental Resources Investigation Program (Grant No. 2022FY101704), the National Natural Science Foundation of China

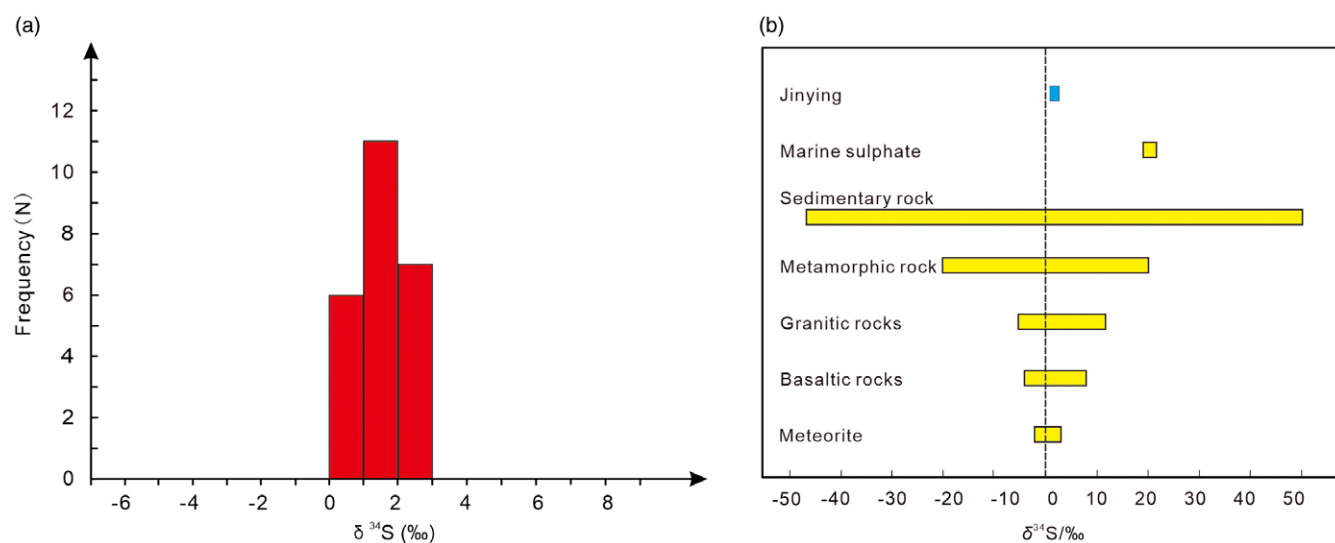


**Figure 9.** (Colour online) Frequency histogram (a) and selected geologically important sulphur reservoirs (b, Wei and Wang, 1988) of  $\delta^{34}\text{S}$  values for pyrite from the Jinying deposit.

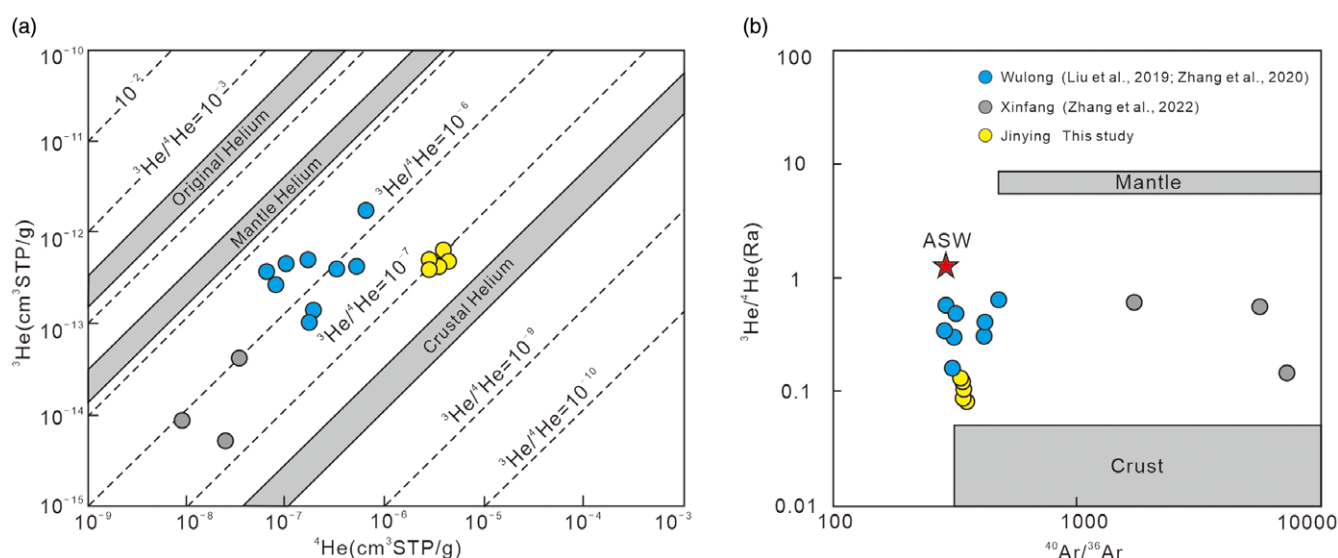


**Figure 10.** (Colour online) Plots of  $^3\text{He}$  versus  $^4\text{He}$  (a, Mamyryn & Tolstikhin, 1984) and  $^3\text{He}/^4\text{He}$  versus  $^{40}\text{Ar}/^{36}\text{Ar}$  (b, Winckler *et al.* 2001) for fluid inclusions in pyrite from the Jinying gold deposit.

(Nos. 42172095, 42072085, 41602075), the Chinese Central Government for Basic Scientific Research Operations in Commonwealth Research Institutes (KK2105) and the Chinese Geological Survey Program (DD20230305). We thank executive editor Dr. Tim Johnson and associate editor Dr. Bo Wang, and Dr. Huan Li and anonymous reviewers for their critical reviews and excellent suggestions that improved this article.

**Competing interests.** The authors declare that they have no known competing financial interests or personal relationships that could have appeared to influence the work reported in this paper.

## References

- Burnard PG, Hu RZ, Turner G and Bi XW (1999) Mantle, crustal and atmospheric noble gases in Ailaoshan gold deposits, Yunnan Province, China. *Geochimica et Cosmochimica Acta* **63**, 1595–604.
- Chen YL, Li H, Zheng CY, Elatikpo SM, Cheng SL and Jiang WT (2022) Ore-forming process of the Haigou gold deposit in the eastern Central Asian Orogenic Belt, NE China: constraints from EPMA and LA-ICP-MS analysis of Au-bearing pyrite. *Resource Geology* **72**, 12304.
- Chen YS (2019) *Ore-forming factors and metallogenic prediction of Banmiaozai gold deposit Jilin Province*. Changchun: Jilin University (in Chinese with English abstract).
- Chen YS, Dong XJ, Liu ZH, Jia ZY, Yu XF, Wu YS and Wang HJ (2020) Metallogenic mechanism of decratonic gold deposit: evidence from diorite porphyrite and fluid inclusions, H-O-S isotope composition of barite in Banmiaozai gold deposit, southern Jilin Province. *Acta Petrologica Sinica* **36**, 2537–57 (in Chinese with English abstract).
- Chu XL, Sun JG, Zhang Y, Liu Y, Xu ZK, Han JL, Zhao CT, Liu YP and Qin KZ (2021) Magmatic constraints on the Ermi porphyry copper mineralization, Northeast China: evidence from zircon U-Pb geochronology, whole-rock geochemistry and Sr-Nd-Hf isotopic geochemistry. *Ore Geology Reviews* **136**, 104294.

- Crowe DE and Vaughan RG** (1996) Characterization and use of isotopically homogeneous standards for in situ laser microprobe analysis of  $^{34}\text{S}/^{32}\text{S}$  ratios. *American Mineralogist* **81**, 187–93.
- Deng J, Yuan WM, Carranza EJM, Yang LQ, Wang CM, Yang LY and Hao NN** (2014) Geochronology and thermochronometry of the Jiapigou gold belt, northeastern China: new evidence for multiple episodes of mineralization. *Journal of Asian Earth Sciences* **89**, 10–27.
- Han JL, Deng J, Zhang Y, Sun JG, Wang QF, Zhang YM, Zhang XT, Liu Y, Zhao CT, Yang F, Wang LL and Lin ZC** (2022) Au mineralization-related magmatism in the giant Jiapigou mining district of Northeast China. *Ore Geology Reviews* **141**, 104638.
- Han JL, Sun JG, Liu Y, Zhang XT, He YP, Yang F, Chu XL, Wang LL, Wang S, Zhang XW and Zhao CT** (2020) Genesis and age of the Toudaoliuhe breccia-type gold deposit in the Jiapigou mining district of Jilin Province, China: constraints from fluid inclusions, H–O–S–Pb isotopes, and sulfide Rb–Sr dating. *Ore Geology Reviews* **118**, 103356.
- Hou KJ, Li YH and Tian YR** (2009) In situ U–Pb zircon dating using laser ablation-multi ion counting-ICP-MS. *Mineral Deposits* **28**, 481–492 (in Chinese with English abstract).
- JBGMR (Jilin bureau of geology and mineral resources)** (1988) *Regional geology of Jilin Province*. Beijing: Geological Publishing House (in Chinese with English abstract).
- Kendrick MA, Burgess R, Patrick RAD and Turner G** (2001) Fluid inclusion noble gas and halogen evidence on the origin of Cu–porphyry mineralizing fluids. *Geochimica et Cosmochimica Acta* **65**, 2651–68.
- Li B, Zang XY, Tao CZ, Ma CS and Ma J** (2015) Genetic type, prospecting criteria and prediction model of the Jinying gold deposit in Jilin Province. *Geology and Resources* **24**, 200–4 (in Chinese with English abstract).
- Li H, Li JW, Algeo TJ, Wu JH and Cisse M** (2018) Zircon indicators of fluid sources and ore genesis in a multi-stage hydrothermal system: The Dongping Au deposit in North China. *Lithos* **314–315**, 463–78.
- Li H, Zhu DP, Algeo TJ, Li M, Jiang WC, Chen SF and Elatikpo SM** (2023) Pyrite trace element and S–Pb isotopic evidence for contrasting sources of metals and ligands during superimposed hydrothermal events in the Dongping gold deposit, North China. *Mineralium Deposita* **58**, 337–58.
- Li JY** (2006) Permian geodynamic setting of Northeast China and adjacent regions: closure of the Paleo-Asian Ocean and subduction of the Paleo-Pacific Plate. *Journal of Asian Earth Sciences* **26**, 207–24.
- Liu J, Li TG and Duan C** (2018) Rb–Sr Isochron Dating and Isotopic Geochemistry Characteristics of the Bajiazi Large Gold Deposit, Jilin Province, China. *Acta Geologica Sinica* **92**, 1432–1446 (in Chinese with English abstract).
- Liu J, Zhang LJ, Wang SL, Li TG, Yang Y, Liu FX, Li SH and Duan C** (2019) Formation of the Wulong gold deposit, Liaodong gold Province, NE China: constraints from zircon U–Pb age, Sericite Ar–Ar age, and H–O–S–He isotopes. *Ore Geology Reviews* **109**:130–43.
- Liu WX, Man YL and Wang XC** (2009) Geology and genesis of the Jinying gold deposit in Jilin Province. *Geology and Resources* **18**, 279–283 (in Chinese with English abstract).
- Ludwig KR** (2003) *Isoplot 3.0—a geochronological toolkit for Microsoft Excel*. Berkeley: Geochronology Center, Spec. Publ., 4:70.
- Mamyrin BA and Tolstikhin IN** (1984) *Helium Isotopes in Nature*. Amsterdam: Elsevier, p. 273.
- Men LJ, Sun JG, Xu YJ, Chai P and Wang HJ** (2016) The research on ore-forming fluid of Banmiaozhi gold deposit in Baishan City in south Jilin Province. *Journal Changchun Institute of Technology (Natural Sciences Edition)* **17**, 83–8 (in Chinese with English abstract).
- Ohmoto H and Rye RO** (1979) Isotopes of sulfur and carbon. In *Geochemistry of Hydrothermal Ore Deposits* (ed HL Barnes), pp. 509–567. New York: Wiley.
- Pei FP, Xu WL, Yang DB, Yu Y, Meng E and Zhao QG** (2011) Petrogenesis of late Mesozoic granitoids in southern Jilin province, northeastern China: geochronological, geochemical, and Sr–Nd–Pb isotopic evidence. *Lithos* **125**, 27–39.
- Sengör AMC, Natal'in BA and Burtman VS** (1993) Evolution of the Altaid tectonic collage and Paleozoic crustal growth in Eurasia. *Nature* **364**, 299–307.
- Sengör AMC and Natal'in BA** (1996) Paleotectonics of Asia: fragments of a synthesis. In *The Tectonic Evolution of Asia* (eds A. Yin and M. Harrison). Cambridge: Cambridge University Press.
- Shen BF, Zhang K and Bi JH** (2020) Geological characteristics of double metallogenic belts in Paleoproterozoic Liaoji active belt. *Mineral Deposits* **39**, 1–18 (in Chinese with English abstract).
- Song MC, Wang L, Song YX, Li J, Wang B, Wei XF, Zhang JJ and Song GZ** (2023) Geometry and origin of supergiant gold deposits in the Jiaodong gold province, eastern China. *Journal of Asian Earth Sciences* **254**, 105744.
- Stuart FM, Burnard PG, Taylor RP and Turner G** (1995) Resolving mantle and crustal contributions to ancient hydrothermal fluids: He–Ar isotopes in fluid inclusions from Dae Hwa W–Mo mineralisation, South Korea. *Geochimica et Cosmochimica Acta* **59**, 4663–4673.
- Su XJ and Zang XY** (2010) Geological characteristics and genetic analysis of Banmiaozhi gold deposit in Baishan City, Jilin Province. *Contributions to Geology and Mineral Resources Research* **25**, 326–30 (in Chinese with English abstract).
- Sun JG, Liu Y, Xu ZK, Xu ZT, Chu XL and Gu AL** (2023) Large scale epithermal mineralization of Late Mesozoic and the constraints of deep geological processes on mineralization in the Continental Margin of NE China. *Journal of Jilin University (Earth Science Edition)* **53**, 651–92 (in Chinese with English Abstract).
- Sun JG, Xing SW, Zheng QD, Huang YW, Yin JF, Liu HW, Wang CF, Ge ZL, Li GH and Chen JQ** (2006) *Geology and Geochemistry of Nonferrous and Noble Metal Deposits, Northeastern China*. Changchun: Jilin University Publishing House, 1–128 (in Chinese with English abstract).
- Sun JG, Zhang Y, Han SJ, Men LJ, Li YX, Chai P and Yang F** (2013) Timing of formation and geological setting of low-sulphidation epithermal gold deposits in the continental margin of NE China. *International Geology Review* **55**, 608–32.
- Tolstikhin IN** (1978) A review: some recent advances in isotope geochemistry of light rare gases. In *Terrestrial Rare Gases* (eds EC Alexander and M Ozima), pp. 27–62. Tokyo: Japan Scientific Society Press.
- Turner G, Burnard P, Ford JL, Gilmour JD, Lyon IC and Stuart FM** (1993) Gruszczynski M, Halliday A. Tracing fluid sources and interactions. *Philosophical Transactions of the Royal Society A Mathematical Physical and Engineering Sciences* **344**, 127–140.
- Wang YX, Gu LX, Zhang ZZ, Wu CZ, Li HM and Yang JD** (2007b) Sr–Nd–Pb isotope geochemistry of rhyolite of the late Carboniferous Dashitou group in eastern Tianshan. *Acta Petrologica Sinica* **23**, 1749–1755 (in Chinese with English Abstract).
- Wang YX, Yang JD, Chen J, Zhang KJ and Rao WB** (2007a) The Sr and Nd isotopic variations of the Chinese Loess Plateau during the past 7 Ma: Implications for the East Asian winter monsoon and source areas of loess. *Palaeogeography, Palaeoclimatology, Palaeoecology* **249**, 351–61.
- Wei JY and Wang GY** (1988) *Isotope Geochemistry*. Beijing: Geological Publishing House (in Chinese).
- Winckler G, Aeschbach-Hertig W, Kipfer R, Botz R, Rübél AP, Bayer R and Stoffers P** (2001) Constraints on origin and evolution of Red Sea brines from helium and argon isotopes. *Earth and Planetary Science Letters* **184**, 671–83.
- Wu FY, Sun DY, Ge WC, Zhang YB, Grant ML, Wilde SA and Jahn BM** (2011) Geochronology of the Phanerozoic granitoids in northeastern China. *Journal of Asian Earth Sciences* **41**, 1–30.
- Wu FY, Yang JH, Xu YG, Wilde SA and Walker RJ** (2019) Destruction of the North China craton in the Mesozoic. *Annual Review of Earth and Planetary Sciences* **47**, 173–95.
- Xing YA, Zhu H, Yang J, Li YF, Feng DC and Liu XP** (2012) Metallogenic stages division of Jinying gold deposit. *Jilin Geology* **31**, 33–4 (in Chinese with English abstract).
- Xu WL, Pei FP, Wang F, Meng E, Ji WQ, Yang DB and Wang W** (2013) Spatial–temporal relationships of Mesozoic volcanic rocks in NE China: constraints on tectonic overprinting and transformations between multiple tectonic regimes. *Journal of Asian Earth Sciences* **74**, 167–93.
- Xuan YF, Dong XJ, Wang CB, Liu ZH, Zhang N, Wang C, Gao Y and Li MQ** (2022) Evidences from zircon U–Pb geochronology, whole-rock geochemistry and Hf isotope of Early Cretaceous magmatic rocks in Baishan area, southern Jilin Province: Constraints on destruction of the North China

- Craton. *Acta Petrologica Sinica* **38**, 2442–66 (in Chinese with English abstract).
- Zeng QD, Wang YB, Yang JH, Guo YP, Yu B, Zhou LL and Qiu HC** (2021) Spatial-temporal distribution and tectonic setting of gold deposits in the Northern margin gold belt of the North China Craton. *International Geology Review* **63**, 941–72.
- Zhai MG** (2013) Secular changes of metallogenic systems link with continental evolving of the North China Craton. *Acta Petrologica Sinica* **29**, 1759–1773 (in Chinese with English abstract).
- Zhang JZ** (2015) *Study on Genesis and Geological and Geochemical Characteristics of Banmiaozhi Gold Deposit in Baishan City, Jilin Province*. Changchun: Jilin University (in Chinese with English abstract).
- Zhang P, Kou LL and Zhao Y** (2022b) Three periods of gold mineralization in the Liaodong Peninsula, North China Craton. *International Geology Review* **64**, 2922–40.
- Zhang P, Kou LL, Zhao Y, Bi ZW, Sha DM, Han RP and Li ZM** (2020) Genesis of the Wulong gold deposit, Liaoning Province, NE China: constrains from noble gases, radiogenic and stable isotope studies. *Geoscience Frontiers* **11**, 547–63.
- Zhang P, Zhao Y, Kou LL, Yang HZ, Sha DM, Yang ZZ, Zhang J and Yu C** (2022a) Genesis of the Xinfang magmatic-hydrothermal gold deposit, Liaodong Peninsula, China: Constraints from pyrite Re-Os isotopes, C, O, S, Pb, Si, He and Ar isotopes. *Ore Geology Reviews* **148**, 105025.
- Zhang XT, Sun JG, Han JL and Feng YY** (2021) Genesis and ore-forming process of the Benqu mesothermal gold deposit in the Jiapigou ore cluster, NE China: Constraints from geology, geochronology, fluid inclusions, and whole-rock and isotope geochemistry. *Ore Geology Reviews* **130**, 103956.
- Zhang XT, Sun JG, Yu ZT and Song QH** (2019) LA-ICP-MS zircon U–Pb and sericite  $^{40}\text{Ar}/^{39}\text{Ar}$  ages of the Songjianghe gold deposit in southeastern Jilin Province, Northeast China, and their geological significance. *Canadian Journal of Earth Sciences* **56**, 607–28.
- Zhang XT, Xu XY, Sun JG, Han JL, Feng YY, Wang S, Liu Y and Chu XL** (2023) Geological, fluid inclusion, and H–O–S–Pb isotopic constraints on the genesis of the Bajiazi mesothermal lode gold deposit in the Jiapigou ore cluster, northeast China. *Ore Geology Reviews* **152**, 105259.
- Zhang Y, Xing SW, Li C, Liang SF, Yu ZT, Du XH, Wang Y, Zhang ZJ and Ma YB** (2017) Early Cretaceous porphyry copper mineralization in northeast China: the Changfagou example. *International Geology Review* **59**, 185–203.
- Zhang Y, Xing SW, Song QH, Wang Y, Yu ZT, Du XH, Ma YB and Zhang ZJ** (2015) Re–Os and U–Pb geochronology of porphyry and skarn types copper deposits in Jilin Province, NE China. *Resource Geology* **65**, 394–404.
- Zhang YB** (2002) *Isotopic Geochronology of the Granitic Magmatic Activity in Yanbian Area*. Changchun: Jilin University (in Chinese with English abstract).
- Zhao GC, Sun M, Wilde SA and Li SZ** (2005) Late Archean to Paleoproterozoic evolution of the North China Craton: key issues revisited. *Precambrian Research* **136**, 177–202.
- Zhao ZX, Xu WJ, Dong GC, Santosh M, Li HB and Chang ZG** (2023) Granitic magmatism associated with gold mineralization: evidence from the Baizhangzi gold deposit, in the northern North China Craton. *Geological Magazine* **160**, 1211–27.
- Zhu RX, Fan HR, Li JW, Meng QR, Li SR and Zeng QD** (2015) Decratonic gold deposits. *Science China: Earth Sciences*, **58**: 1523–37.